Ceramics International 49 (2023) 11589–11599

Contents lists available at ScienceDirect

Ceramics International

journal homepage: www.elsevier.com/locate/ceramint

In situ facile one-step solvothermal synthesizing hexagonal ammonium tungsten bronze $(NH_4)_{0.33}WO_3$ to tap NIR light absorption ability by controlling crystallinity

Te Hu [a,*], Dong Fang [b,**], Ian R. Baxendale [c], Lang Zhang [b], Qihang Liu [b], Jianhong Yi [b,***]

[a] Faculty of Science, Kunming University of Science and Technology, South Jingming Road, Kunming, 650500, China
[b] Faculty of Materials Science and Engineering, Kunming University of Science and Technology, Xuefu Road, Kunming, 650093, China
[c] Department of Chemistry, Durham University, South Road, Durham, DH1 3LE, United Kingdom

ARTICLE INFO

Keywords:
Solvothermal
$(NH_4)_{0.33}WO_3$
NIR absorption
Crystallinity
The first principle

ABSTRACT

Tungsten bronze (TB) has potentially high visible light transparency and excellent near-infrared (NIR) shielding ability. To fully dig out the concealed optical properties of TB with specific chemical components, in this work, hexagonal ammonium tungsten bronze (*h*-ATB) $(NH_4)_{0.33}WO_3$ was fabricated by a one-step solvothermal reaction. Through X-ray diffractometer (XRD), scanning electron microscope (SEM), transmission electron microscopy (TEM), X-ray photoelectron spectroscopy (XPS), and ultraviolet–visible–near infrared (UV–vis–NIR) spectroscopy to characterize *h*-ATB, which unraveled that controlling crystallinity could adjust the optical property of *h*-ATB. In particular, when the crystallinity of the *h*-ATB is over 95%, it exhibits the attractive NIR light shielding capability, which is in line with the predicted optical property via the first principle calculation based on density functional theory (DFT). Given the result, this work can provide a feasible research idea to explore the hidden optical properties of TB.

1. Introduction

The edges of the WO_6 octahedra form triangular, quadrangular, pentagonal, or hexagonal channels [1], therefore nonstoichiometric tungsten bronzes (TB) are prepared by doping various cations in these open tunnels. As known, the general formula of TB is M_xWO_3, where M represents alkali metal ions, alkaline earth metal ions, rare earth metal ions, or ammonium ions, whereas, due to the distinctive radiuses and binding energies of these ions theoretical range of x is from 0 to 1 [2–5]. Because of the cations entering the channels of the WO_3, partial W^{6+} is reduced to W^{5+} or W^{4+}, therefore, tungsten ions with mixed valence exist in the TB.

With these particular structural characteristics and doping cations, TB displays attractive properties, such as electronic, magnetic, and optical properties [6–11], superconductivity [12,13], gas sensing [14,15], absorption [16], photocatalysis [17], medicine [18], electrochemical and thermochromic properties [19–21], and so on.

A spate of the report [22–24] discusses metal ions as doping elements more than non-metal ions to prepare TB. Consequently, ammonium ion is selected to dope in tungsten oxide to investigate the latent optical properties of the corresponding TB. Although employing ammonium ion for synthesizing ammonium tungsten bronze $(NH_4)_xWO_3$ (ATB) has been reported [25–27], it lacks systematic investigation from theoretical calculation to experimental preparation and characterization analysis.

Szilàgyi et al. [25] produced ammonium tungsten bronze (ATB) by annealing ammonium paratungstate tetrahydrate (APT, $(NH_4)10[H_2W_{12}O_{42}]\bullet 4H_2O$) in H_2 at 400 °C for 6 h. But the dopant element in the ATB includes not only ammonium ion (NH_4^+) but also NH_3 and H_2O formed as $(NH_4)_{0.08}(NH_3)_{0.04}(H_2O)_{0.09}WO_{2.93}$, thus, it could not be strictly identified as ATB. The authors tried to explain the possibility of NH_3 and H_2O existing in the hexagonal channels by TG (Thermogravimetric Analysis)/DTA (Differential Thermal Analysis) and NMR (Nuclear Magnetic Resonance). Nevertheless, these analyses were insufficient to explicate what kind of chemical energy binding mode made NH_3 and H_2O stabilize in these channels and how the proportions of elements were determined in the compound. Therefore, the

* Corresponding author.
** Corresponding author.
*** Corresponding author.
E-mail addresses: hutete@kust.edu.cn (T. Hu), fangdong@kmust.edu.cn (D. Fang), yijianhong@kmust.edu.cn (J. Yi).

https://doi.org/10.1016/j.ceramint.2022.12.006
Received 24 August 2022; Received in revised form 20 November 2022; Accepted 1 December 2022
Available online 5 December 2022

mechanism of chemical synthesis remained unknown. Ou et al. [26] synthesized ammonium tungsten bronze ($(NH_4)_xWO_3$) but via a two-step solvothermal method. The tungsten trioxide (WO_3) powders were prepared in advance at 200 °C for 12 h using sodium tungstate dihydrate ($Na_2WO_4{\cdot}2H_2O$) and sulfuric acid (H_2SO_4), then mixed with the WO_3 and thiourea (CH_4N_2S) under the same solvothermal treatment to obtain $(NH_4)_xWO_3$. However, whether the intermediate 5 $(NH_4)_2O{\cdot}12WO_3{\cdot}nH_2O$ appeared during the reaction procedure and the value x in $(NH_4)_xWO_3$ is unclear. Luo et al. [27] prepared hexagonal $(NH_4)_xWO_3$ by solvothermal treatment at 200 °C for 12 h selecting $Na_2WO_4{\cdot}2H_2O$, CH_4N_2S, and $C_6H_8O_7{\cdot}H_2O$ as raw materials, nevertheless, if solvothermal time was less than 12 h, several side products appeared leading to experimental instability and repeatability restrictions. Moreover, whether ions release and regenerate according to the listed equations from starting materials in a solution leads to the rationality of the chemical reaction mechanism being uncertain.

In this study, WO_3 and ATB were prepared by an effortless solvothermal reaction, a corresponding chemical mechanism was concisely deduced, and the proportion x in $(NH_4)_xWO_3$ was precisely determined. It is an intriguing discovery that the optical property of ATB can be controlled by adjusting crystallinity and that when the crystallinity exceeds 95%, ATB can obtain the NIR shielding ability. Band structures, electronic structures, dielectric functions, and optical properties of *h*-WO_3 and *h*-ATB have been computed based on density functional theory (DFT). Phases, morphologies, size, chemical composites, valence states, and optical properties of products were respectively characterized by XRD (X-ray diffractometer, Cu Kα Radiation, MiniFlex600, Rigaku, Japan), SEM (scanning electron microscope, Nova Nano450, FEI, USA), TEM (transmission electron microscopy, Tecnai G2 TF30, FEI, USA), XPS (X-ray photoelectron spectroscopy, HPI500 VersaProbeII, ULVAC, Japan), and UV–vis–NIR (ultraviolet–visible–near infrared spectroscopy, UV-1700PC, Mrcy, China).

2. Results and discussion

2.1. Simulation calculation

The calculations were carried out by employing the plane-wave basis function in the framework of density functional theory (DFT) [28,29] with ultrasoft pseudopotential [30] and generalized gradient approximation Perdew-Burke-Ernzerhof (GGA-PBE) [31]. The cut-off energy was set at 550 eV. The valence states in the calculations were O: $2s^2\ 2p^4$, W: $6s^2\ 5d^4$, and NH_4^+: sp^3 (To the NH_4^+ Lewis structure, in an excited state, there are four unpaired electrons from an N atom, one from the *s* orbit and the other three from the *p* orbit under hybridization with four single electrons from four H atoms, thus a new hybrid orbital sp^3 is formed.). To invoke geometry optimization, 3 × 3 × 3 K-points mesh grid, 2 × 2 × 2 supercell, energy 2×10^{-5} eV/atom, max force 0.05 eV/Å, max stress 0.1 GPa, and max displacement 0.002 Å were set. Based on the optimized structures, band and electron structures and optical properties of *h*-WO_3 and *h*-ATB were calculated.

Fig. 1 represents the 2 × 2 × 2 supercell structure of *h*-WO_3 and *h*-ATB along with the c-axis perspective view and comparative structural data as shown in Tables 1 and 2.

2.1.1. Electronic properties

Figs. 2 and 3 demonstrate the band structures and the densities of states of *h*-WO_3 and *h*-ATB. *h*-WO_3 band structure agrees with what was obtained by Yang *el al* [32]. and Jin *el al* [33]. Fig. 2(a) shows that the conduction band minimum (CBM) and valence band maximum (VBM) of *h*-WO_3 are located, respectively, at the Z and G points, relating to the indirect transition and determining a band gap of 1.943 eV. Fig. 3(a) illustrates that the conduction energy levels around 0eV∼5eV mainly consist of W 5*d* states with little O 2*p* states, therefore, W 5*d* states decide CBM; and the top valence energy levels around −7.5eV∼0eV mainly consist of O 2*p* states with little W 5*d* states, thus, O 2*p* states contribute to VBM. From this, it can be seen that the electronic transition under photon excitation from O 2*p* states to W 5*d* states determines the theoretical optical properties of *h*-WO_3.

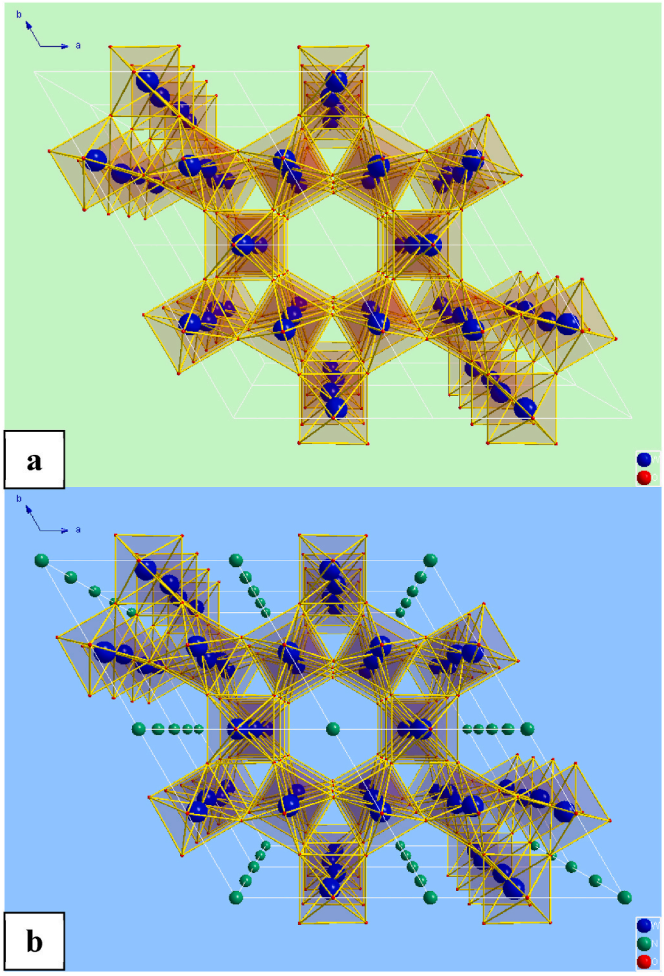

Fig. 1. Perspective view on 2 × 2 × 2 supercell structure of *h*-WO_3 (a) and *h*-ATB (b) along with the c-axis. W atom, O atom, and NH_4^+ group ion is individually labeled by blue, red, and green balls. (For interpretation of the references to colour in this figure legend, the reader is referred to the Web version of this article.)

Comparatively, dopant NH_4^+ in *h*-ATB brings its energy levels into the band gap, leading CB and VB to combine as a wide valence band; thus, the Fermi level locates inside the VB, and the system is converted from semiconductor to metallic-like [34], as shown in Fig. 2(b). Fig. 3(b) depicts dopant NH_4^+ *sp* states that have been hybridized with W 5*d* states and O 2*p* states to generate new states inside the band gap.

2.1.2. Optical property

The dielectronic function of photoelectronic materials is as the following equation:

$$\varepsilon(\omega) = \varepsilon_1(\omega) + i\varepsilon_2(\omega) \tag{1}$$

In the equation, the imaginary part $\varepsilon_2(\omega)$ is obtained from the momentum matrix elements between the occupied and empty electronic states with the local field in the random phase approximation (RPA) [35], and the real part $\varepsilon_1(\omega)$ of the dielectric function is calculated using the Kramers–Krönig relation [36].

Fig. 4 gives the dielectronic functions of *h*-WO_3 and *h*-ATB. The peaks on the imaginary part $\varepsilon_2(\omega)$ red lines there are at 3.66eV, 8.39eV, 20.11eV and 42.26eV from *h*-WO_3 in Fig. 4(a) and at 0eV, 4.39eV, 11.52eV, 20.16eV and 42.30eV from *h*-ATB in Fig. 4(b). The maximum

Table 1
Phase data of hexagonal WO_3 and ATB.

	Space group	a	B	c	α	β	γ
***h*-WO$_3$**	P 63 c m (185)	7.5073 Å	7.7275 Å	7.7275 Å	90 °C	90 °C	120 °C
***h*-ATB**	P 63/m c m (193)	7.3920 Å	7.5120 Å	7.5120 Å	90 °C	90 °C	120 °C

Table 2
Atomic parameters of hexagonal WO_3 and ATB.

	Atom	Wyckoff	Site	x/a	y/b	z/c
***h*-WO$_3$**	W0	6c	..m	0	0.48316	0.26103
	O1	12d	1	0.20984	0.42598	0.75103
	O2	6c	..m	0	0.49862	0.50288
***h*-ATB**	O1	12j	m..	0.216	0.423	1/4
	W1	6g	m2m	0.48241	0	1/4
	O2	6f	..2/m	1/2	0	0
	(NH_4^+)1	2b	−3.m	0	0	0

peak of *h*-WO_3 at 3.66eV is attributed to the interband transition from O 2*p* states on the VBM to the W 5*d* states on the CBM as shown in Fig. 4(a). As can be seen in Fig. 4(b), the energy is reduced to 0eV because the doping NH_4^+ group ion increases the free carrier concentration and thus decreases the mean free path of electrons, which is approximate metallic-phase-like [34]. The corresponding values of intersection points between the real part $\varepsilon_1(\omega)$ blue line and black dot lines represent plasma energies, deciding the NIR shielding capability of *h*-ATB [37,38].

Based on the dielectric function, transmittance $T(\omega)$ can be obtained according to the reflectivity $R(\omega)$ and absorption coefficient $\alpha(\omega)$ by the following formulas [39–41]:

$$R(\omega)=\left|\frac{\sqrt{\varepsilon_1(\omega)+i\varepsilon_2(\omega)}-1}{\sqrt{\varepsilon_1(\omega)+i\varepsilon_2(\omega)}+1}\right|^2 \tag{2}$$

$$\alpha(\omega)=\sqrt{2}\omega\left[\sqrt{\varepsilon_1^2(\omega)+\varepsilon_1^2(\omega)}-\varepsilon_1(\omega)\right]^{1/2} \tag{3}$$

$$T(\omega)=\frac{(1-R)^2\ exp(-\alpha d)}{1-R^2\ exp(-2\alpha d)} \tag{4}$$

where *d* is the thickness of the material film which set as 20 nm in the calculation.

Fig. 5 indicates the calculated optical properties of *h*-WO_3 and *h*-ATB. In the UV range, *h*-WO_3 blocks 62% within 380 nm, which is higher than 39% of *h*-ATB, and the maximum transmittance in the visible range for *h*-WO_3 is 98%, which is similar to 94% of *h*-ATB. Although *h*-WO_3 lacks NIR shielding capability, *h*-ATB performs NIR-preventing ability starting

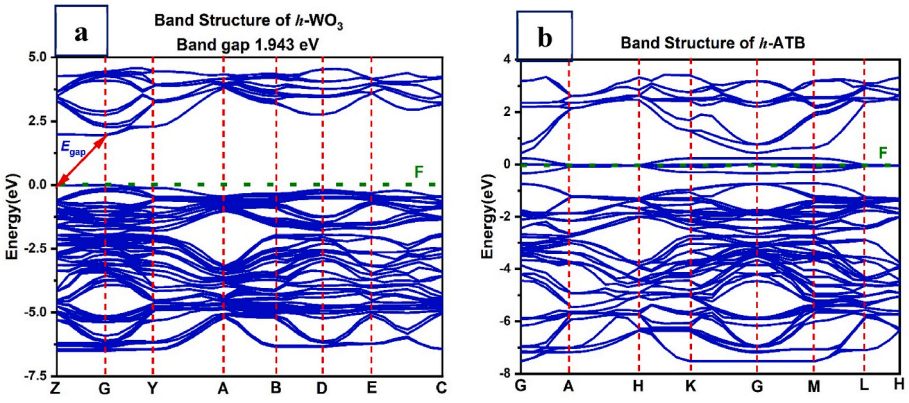

Fig. 2. Band structures of *h*-WO_3 (a) and *h*-ATB (b).

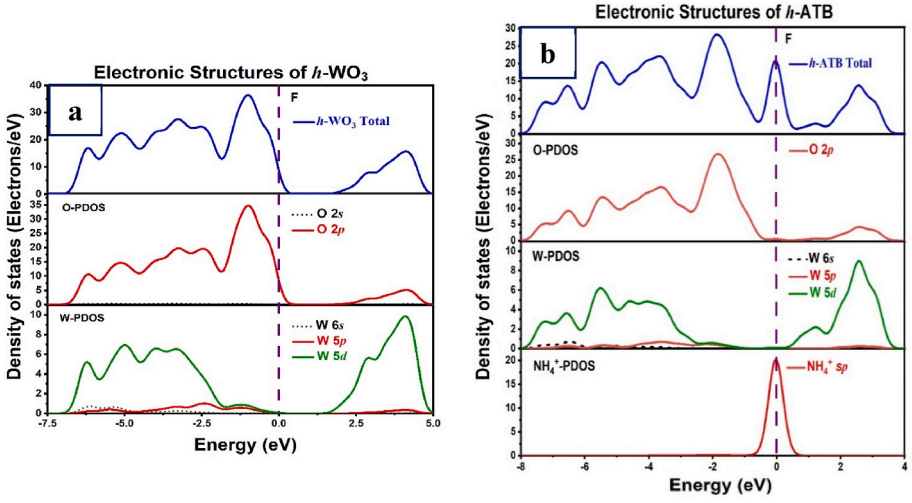

Fig. 3. Electronic structures of *h*-WO_3 (a) and *h*-ATB (b).

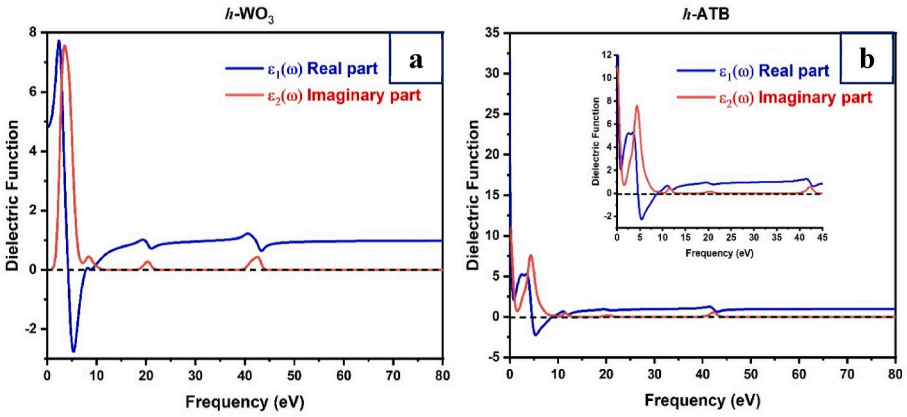

Fig. 4. The dielectric function of *h*-WO_3 and *h*-ATB.

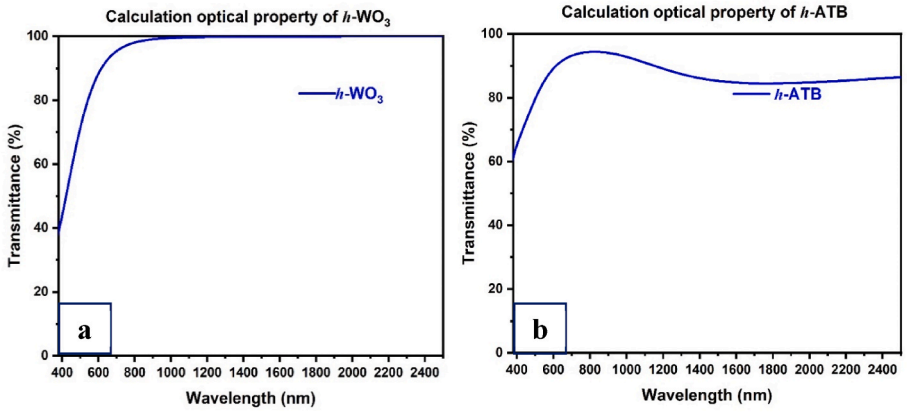

Fig. 5. Theoretical optical property of (a) *h*-WO_3 and (b) *h*-ATB.

at 800 nm owing to doped NH_4^+ making plasma frequencies and energies change.

2.2. Experiment

2.2.1. Process

The one-step solvothermal reaction program for preparing *h*-ATB in

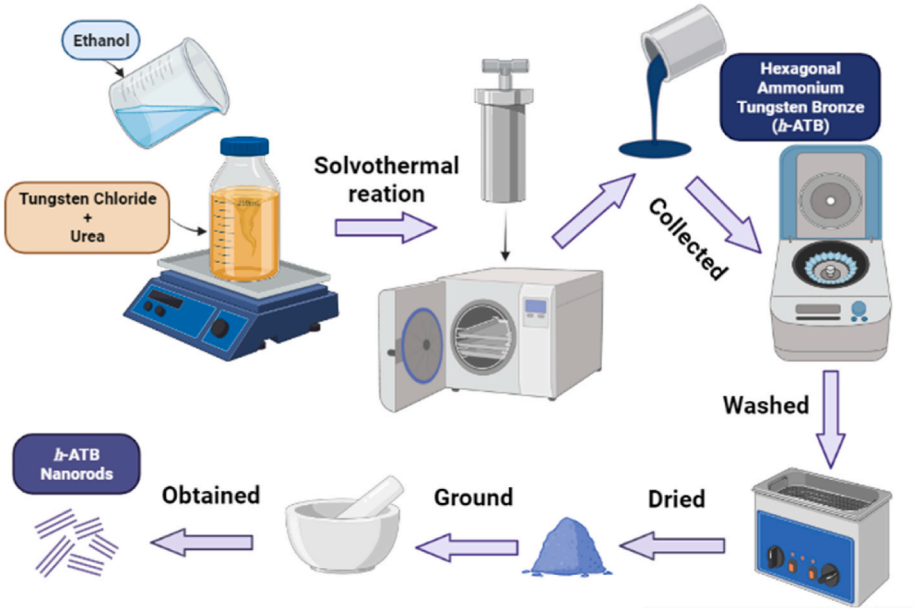

Fig. 6. Experimental process of preparing *h*-ATB.

situ is shown in Fig. 6 (the same process is used to synthesize *h*-WO_3 and β-WO_3). The chemical reagents used in this experiment were of analytical-grade purity, with tungsten chloride (WCl_6) acting as a tungsten source and urea ($CO(NH_2)_2$) providing NH_4^+ group ion. The molar ratios of tungsten chloride to urea (W^{6+}/NH_4^+) of 1:0.1, 1:0.165, 1:0.22, 1:0.33, 1:0.44, 1:0.55, 1:0.66, and 1.077 and the solvothermal times of 2 h, 4 h, 6 h, 8 h, 12 h, 16 h, 20 h, and 24 h, were chosen to investigate the effects of these variables on the crystalline and optical properties of *h*-ATB.

The detailed process was as follows: a certain molar ratio of tungsten chloride to urea was dissolved in 80 mL of ethanol, keeping mixed solution molarity at 15 mM while stirring for 40min. The mixture was poured into a 100 mL Teflon-lined autoclave and heated in an oven at 200 °C for a specific solvothermal time. After cooling the mixture to ambient temperature, the blue flocs were collected by a centrifuge for 5min at 8000 rad/min and washed by an ultrasonic disperser with ultrapure water for 10min, recycling the process three times, then the blue deposit was dried in the oven at 60 °C for 12 h. The dried solid was ground with mortar for half an hour, yielding a blue-gray *h*-ATB nanomaterials powder.

2.2.2. Mechanism of chemical reaction

Tungsten chloride (WCl_6) was chosen as the raw material because it is likely to undergo elementary reactions, thereby eliminating potential intermediates, simplifying chemical mechanism analysis, and improving product synthesis possibilities. Urea ($CO(NH_2)_2$) was used as the raw material to produce NH_4^+. Meanwhile, compared with other alcohols, tungsten chloride and urea are more apt to be soluble in ethanol (C_2H_5OH), which occurs through a dehydration condensation reaction to form diethyl ether and water. Based on the preceding analysis, reasonable equations for the solvothermal reaction to prepare *h*-ATB are as follows:

$$2CH_3CH_2OH \rightarrow CH_3CH_2OCH_2CH_3 + H_2O \quad (5)$$

$$CO(NH_2)_2 + H_2O = CO_2\uparrow + 2NH_3\uparrow \quad (6)$$

$$NH_3 + H_2O \rightleftharpoons NH_3{\cdot}H_2O \quad (7)$$

$$NH_3{\cdot}H_2O \rightleftharpoons NH_4^+ + OH^- \quad (8)$$

$$WCl_6 + 3H_2O = WO_3 + 6HCl \quad (9)$$

$$WO_3 + NH_3{\cdot}H_2O \rightarrow (NH_4)_{0.33}WO_3 + H_2O \quad (10)$$

2.3. Characterization

2.3.1. XRD analysis

Fig. 7 shows all XRD patterns of *h*-WO_3, β-WO_3, and *h*-ATB, and the total reflection peaks are indexed to *h*-WO_3 (PDF#33–1387), β-WO_3 (PDF#20–1324), and *h*-ATB (PDF#42–0542). *h*-WO_3 and β-WO_3 were synthesized using WCl_6 and ethanol at 200 °C for 20 h with respective solution molarities of 15 mM and 30 mM in Fig. 7(a) *h*-ATB was prepared in two contrastive experimental conditions by employing WCl_6, urea, and ethanol. One approach involved changing the molar ratio of W^{6+}/NH_4^+ at 200 °C for 24 h in Fig. 7(b), and another method included varying the solvothermal time at 200 °C with a constant molar ratio of

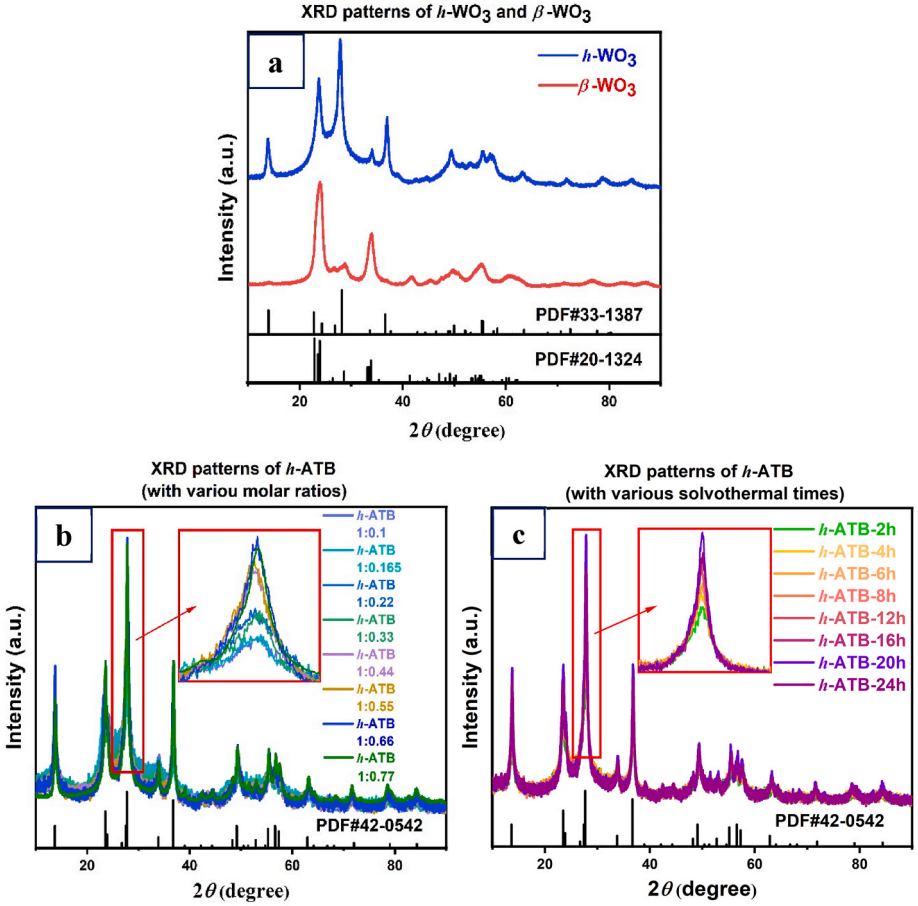

Fig. 7. XRD patterns of (a) *h*-WO_3 and β-WO_3 prepared at 200 °C for 24 h with 15 mol/L and 30 mol/L solution molarity, (b) *h*-ATB prepared at 200 °C for 24 h with various molar ratios of W^{6+}/NH_4^+, and (c) *h*-ATB prepared at 200 °C for various solvothermal times with 1:0.66 M ratio of W^{6+}/NH_4^+ and solution molarity of 15 mol/L.

1:0.66 of W^{6+}/NH_4^+ in Fig. 7(c).

The phase transition of tungsten oxide from hexagonal to orthorhombic occurs. It could be conjectured that the solution system absorbs more thermal energy under high solution molarity at the same solvothermal condition, which drives WO_3 octahedra to rotate in the crystal structure to convert axes at 120° to each other to be mutually perpendicular.

Fig. 8 illustrates the crystallinities of products under the two solvothermal conditions. One of them was raising the molar ratio of W^{6+}/NH_4^+ from 1:0.1 to 1:0.77, which resulted in the crystallinities of *h*-ATB gradually increasing and trending to steady after 1:0.66 as shown in Fig. 8(a). It could be surmised that excessive ammonium ion NH_4^+ covering the surfaces of nanoparticles weakens the capillary force between nanoparticles and stabilizes solute and thermal energy on crystalline planes transferring to gradually retard crystal growth.

Another option was to prolong the solvothermal time from 2 h to 24 h as shown in Fig. 8(b). Although the crystallinities of *h*-ATB increased with time, the crystallinity of *h*-ATB at 24 h was lower than that of *h*-ATB at 20 h. It is possible to hypothesize that over 20 h, the consistently enhancing crystallization driving force may cause the crystal growth at the interface between the solution and solid to lose stability, bringing about a decrease in crystallinity.

The crystallinities of *h*-ATB were calculated from XRD patterns data with the following equation:

$$Crystallinity = \frac{Area\ of\ crystalline\ peaks}{Area\ of\ all\ peaks\ (crystalline\ and\ amorphous)} \times 100 \qquad (11)$$

2.3.2. XPS analysis

The chemical composition and chemical state of the *h*-WO_3 and the *h*-ATB nanocrystals were examined by X-ray photoelectron spectroscopy (XPS) and the results are shown in Fig. 9.

Fig. 9(a) and (b) indicate the full range of XPS spectra of the *h*-WO_3 and the *h*-ATB nanocrystals. Peaks at binding energies corresponding to O, W, and N (NH_4^+) elements were observed, and no impurities were detected in these spectra.

For N 1s (N 1s represents NH_4^+ because XPS is difficult to detect the signal of H [42]), the peak energy of N 1s in *h*-ATB at 401.8eV comparing upshot with *h*-WO_3 without an N atom is illustrated in Fig. 9 (c).

The highest point of the photoelectrons from O 1s is around 530.59eV (*h*-WO_3) and 530.43eV (*h*-ATB), which is assigned to the oxygen atoms bonding with the tungsten atom in the octahedra as shown in Fig. 9(d) and (e). Attributing to doping NH_4^+, W^{6+} is reduced to W^{5+} and W^{4+}, leading to oxygen vacancies [43–45] increasing in the crystal structure, therefore, the integration area is shrunk from *h*-WO_3 to *h*-ATB.

Fig. 9(f) demonstrates the complex energy distributions of W 4*f* photoelectrons. The W 4*f* core-level spectra could be fitted into one doublet associating with the valence state of W^{6+} in the *h*-WO_3, and the main peaks have W $4f_{5/2}$ at 37.52eV and W $4f_{7/2}$ at 35.35eV.

However, due to NH_4^+ existing in the *h*-ATB, the W atoms are in these three oxidation states: W^{6+}, W^{5+}, and W^{4+} in Fig. 9(g), thus the W 4*f* core-level spectra could be fitted into three spin-orbit doublets.

The first doublet of having W $4f_{5/2}$ at 37.80eV and W $4f_{7/2}$ at 35.73eV was attributed to W^{6+}. As for the second doublet, the lower energy at 36.83eV for W $4f_{5/2}$ and 34.99eV for W $4f_{7/2}$ was from W^{5+}. Furthermore, the third doublet, obtained at 41.23eV and 38.58eV from the emission of W $4f_{5/2}$ and W $4f_{7/2}$ core-levels, was derived from W^{4+}. According to the integration areas proportion between nitrogen (N1s) and tungsten core-level (W 4*f*) in *h*-ATB and atomic sensitivity factors, the value *x* in $(NH_4)_xWO_3$ was calculated as 0.33, wherefore the chemical formula of the ammonium tungsten oxide could be represented as $(NH_4)_{0.33}WO_3$.

2.3.3. SEM and TEM analysis

Fig. 10 shows SEM, TEM, HRTEM, and SEAD (selected area electron diffraction) pattern images of *h*-ATB, which was synthesized at 200 °C for 20 h with a W^{6+}/NH_4^+ molar ratio of 1:0.66 and the solution molarity of 15 mM. The SEM images in Fig. 10(a) and (b) indicate that the product in the aggregative state is predominantly composed of nanorods with few nanoparticles. The TEM image in Fig. 10(c) demonstrates these nanorods are around 10–25 nm in diameter and 30–50 nm in length. And corresponding SAED patterns are shown in Fig. 10(d), indicating that the Miller index of the ring set has been indexed according to the *h*-ATB crystal phase, which is in agreement with XRD in Fig. 7(b) and (c). The HRTEM image in Fig. 10(e) illustrates the single crystalline nature of prepared *h*-ATB nanorods with a lattice spacing of 0.3703 nm and 0.3125 nm, which are respectively corresponding to the (002) and (200) crystal planes shown in Fig. 10(f).

2.3.4. Optical property measurement

Fig. 11 demonstrates the transmittance spectra of *h*-WO_3, *β*-WO_3, and *h*-ATB. These mixed solutions for optical characterization were prepared by ultrasonically diffusing and magnetically stirring these sample powders in ethanol for 20 min.

Fig. 11(a) shows that *h*-WO_3 and *β*-WO_3 have similar optical characteristics, effectively blocking UV around 300 nm, transmittance gradually increasing in the visible light range from 380 nm to 780 nm, but failing to shield on NIR light, which is accordant with previously calculated results in Fig. 5(a).

Fig. 11(b) and (c) illustrate that basically, *h*-ATB has optical properties similar to these of *h*-WO_3 and *β*-WO_3 from UV to visible light, and the optical curve distribution is related to crystallinity in Fig. 8(a) and (b). However, it is intriguing to note that when the crystallinity of *h*-ATB

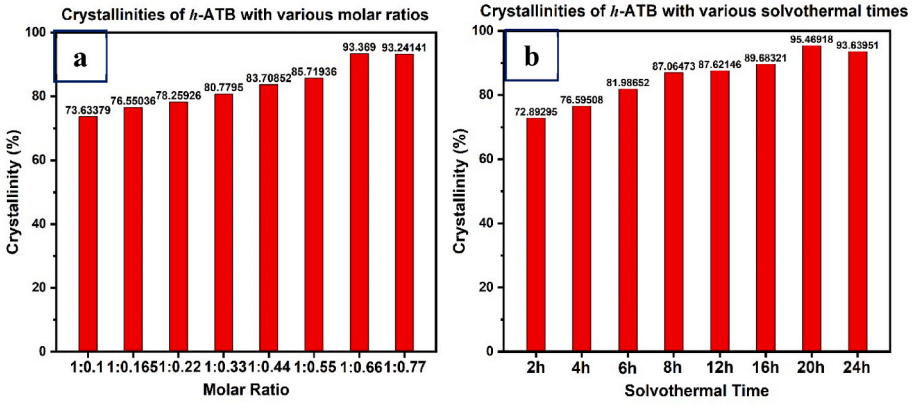

Fig. 8. (a) crystallinity of *h*-ATB prepared at 200 °C for 24 h under solution molarity of 15 mol/L with various molar ratios of W^{6+}/NH_4^+ and (b) crystallinity of *h*-ATB synthesized at 200 °C for various solvothermal times with the molar ratio 1:0.66 of $W^{6+}/NH_4^+$and solution molarity of 15 mol/L.

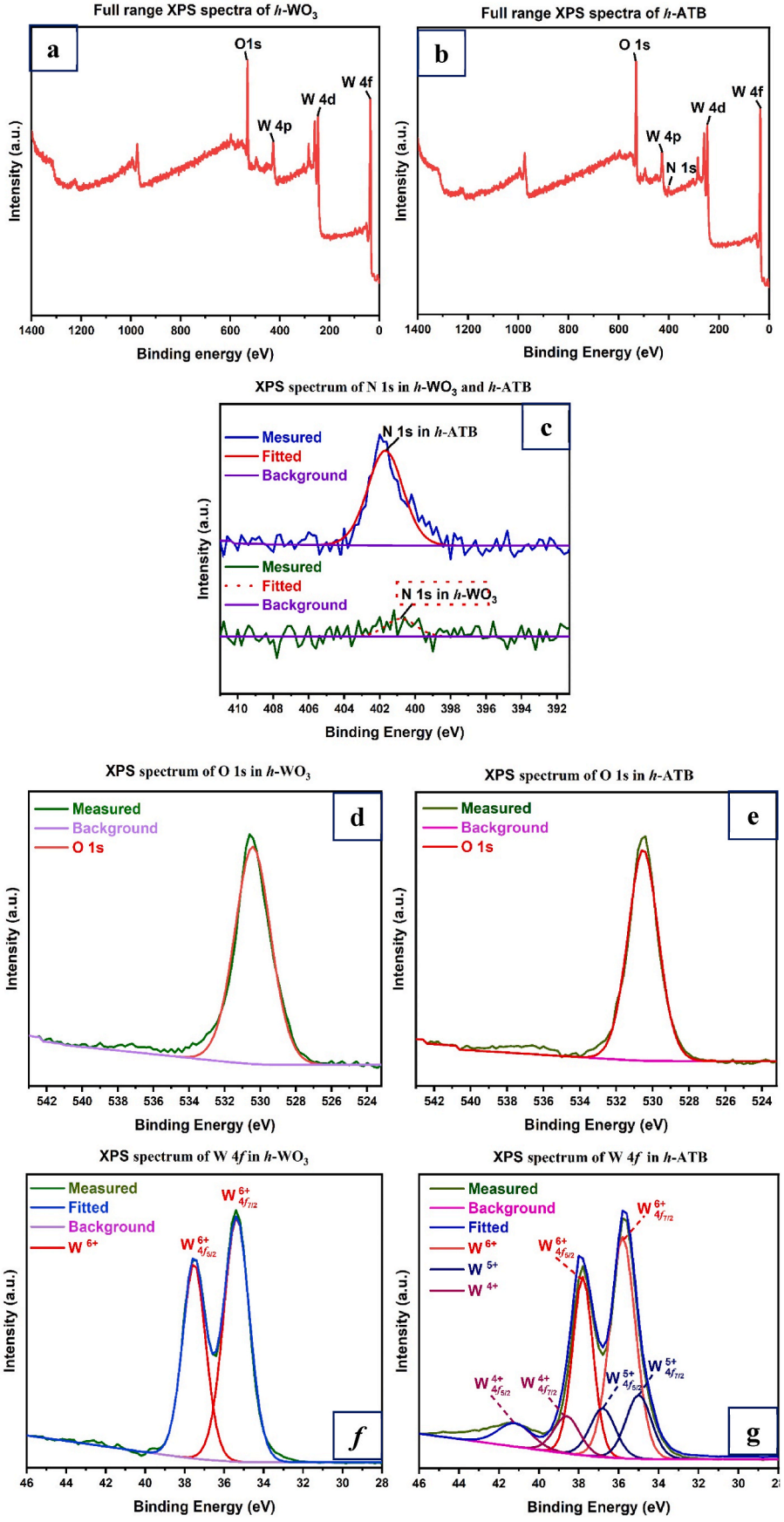

Fig. 9. Full range XPS spectra of (a) *h*-WO_3 and (b) the *h*-ATB, (c) N 1s XPS spectrum of *h*-WO_3 and the *h*-ATB, O 1s XPS spectrum of (d) *h*-WO_3 and (e) the *h*-ATB, W 4*f* XPS spectrum of (f) *h*-WO_3 and (g) the *h*-ATB.

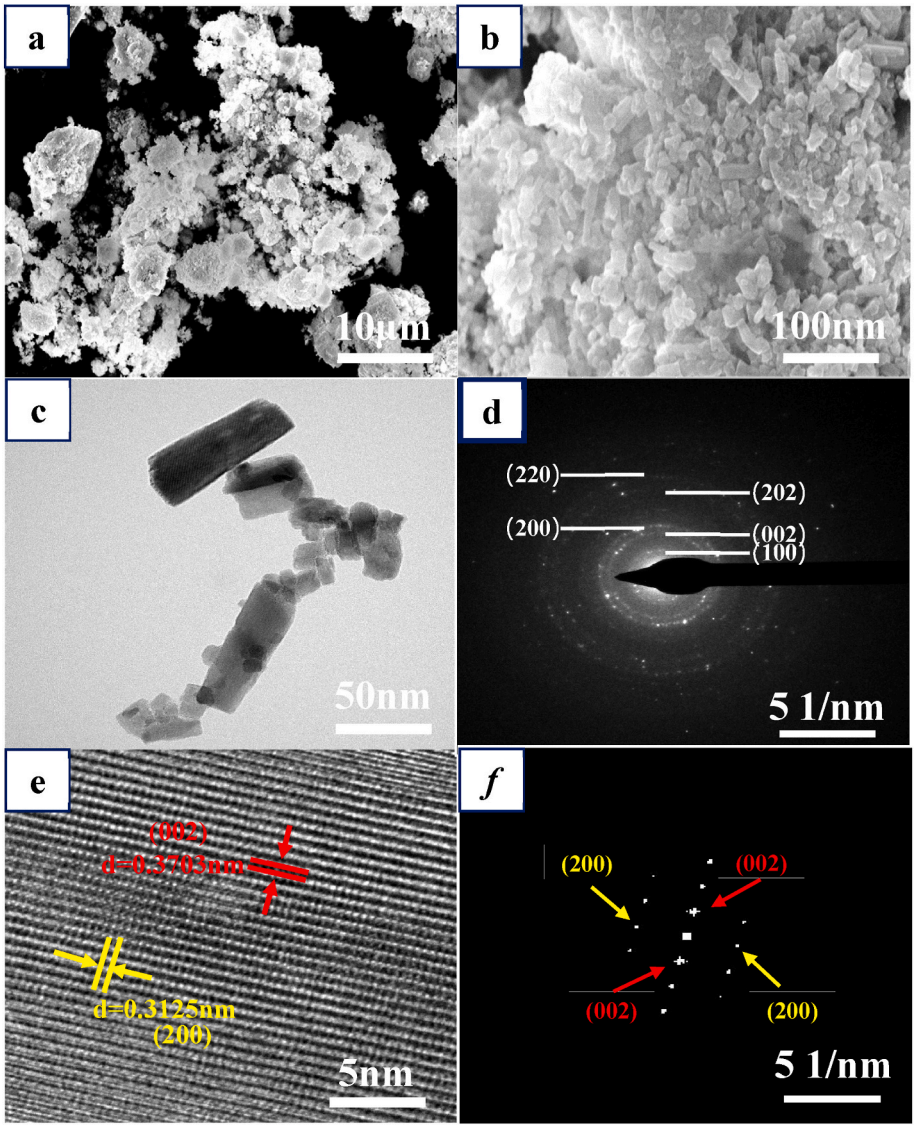

Fig. 10. (a) and (b) SEM images of *h*-ATB, (c) TEM image and (e) HRTEM image of *h*-ATB, (d) and (f) corresponding SAED patterns respectively indexing to polycrystalline and single crystal *h*-ATB.

is increased up to 95% in Fig. 8 (b), the transmittance peak of *h*-ATB appears at 800 nm and exhibits a shielding feature on NIR light as shown in Fig. 11(c), which complies with the pre-computed consequence in Fig. 5(b).

It can be surmised that increasing crystallinity will promote photon penetrating depth on lattice planes, guiding and intensifying photon-electron oscillations between crystal faces; meanwhile, increased electron concentration interacting with SPPs (surface plasmon polaritons) due to doping NH_4^+ will further boost plasmon resonance frequency, which makes it possible to scoop out the potential shielding properties of NIR light of *h*-ATB. Based on analyses from Figs. 8 and 11, the assumption is confirmed that a connection between the optical property and crystallinity of *h*-ATB exists.

Based on the Drude model and Kramers–Krönig relation, the wave vector of propagating surface plasmon polaritons on the interface of semiconductor media and air along a horizontal direction is approximated by the following formula:

$$k=\frac{\omega}{c}\sqrt{\frac{\varepsilon_a\varepsilon_d}{\varepsilon_a+\varepsilon_d}}=\frac{\omega}{c}\sqrt{\frac{\varepsilon_a\varepsilon_d^{'}}{\varepsilon_a+\varepsilon_d^{'}}}+i\frac{\omega}{c}\left(\frac{\varepsilon_a\varepsilon_d^{'}}{\varepsilon_a+\varepsilon_d^{'}}\right)^{3/2}\frac{\varepsilon_d^{''}}{2(\varepsilon_d^{'})^2} \tag{12}$$

Where $\varepsilon_d^{'}$ and $\varepsilon_d^{''}$ are the real and imaginary parts of the dielectric function of the semiconductor separately, and ε_a represents the dielectric function of the air. The real part $k^{'}=\frac{\omega}{c}\sqrt{\frac{\varepsilon_a\varepsilon_d^{'}}{\varepsilon_a+\varepsilon_d^{'}}}$ decides the wavelength of SPPs (λ_{SPPs}) which is expressed by the following equation [46]:

$$\lambda_{SPPs}=\frac{2\pi}{k^{'}}=\frac{2\pi c}{\omega}\sqrt{\frac{\varepsilon_a+\varepsilon_d^{'}}{\varepsilon_a\varepsilon_d^{'}}}=\lambda_0\sqrt{\frac{\varepsilon_a+\varepsilon_d^{'}}{\varepsilon_a\varepsilon_d^{'}}} \tag{13}$$

The imaginary part $k''=\frac{\omega}{c}\left(\frac{\varepsilon_a\varepsilon_d^{'}}{\varepsilon_a+\varepsilon_d^{'}}\right)^{3/2}\frac{\varepsilon_d^{''}}{2(\varepsilon_d^{'})^2}=k_0\left(\frac{\varepsilon_a\varepsilon_d^{'}}{\varepsilon_a+\varepsilon_d^{'}}\right)^{3/2}\frac{\varepsilon_d^{''}}{2(\varepsilon_d^{'})^2}$ determines propagation length of SPPs (L_{SPPs}) using the following equation:

$$L_{SPPs}=\frac{1}{2k''}=\lambda_0\frac{(\varepsilon_d^{'})^2}{2\pi\varepsilon_d^{''}}\left(\frac{\varepsilon_a+\varepsilon_d^{'}}{\varepsilon_a\varepsilon_d^{'}}\right)^{3/2} \tag{14}$$

The penetration depth of SPPs (δ_d) in the semiconductor is given by:

$$\delta_d=\frac{1}{k_0}\left|\frac{\varepsilon_a+\varepsilon_d^{'}}{(\varepsilon_d^{'})^2}\right| \tag{15}$$

Simplifying equations (14) and (15) with equation (13) as the following formulas:

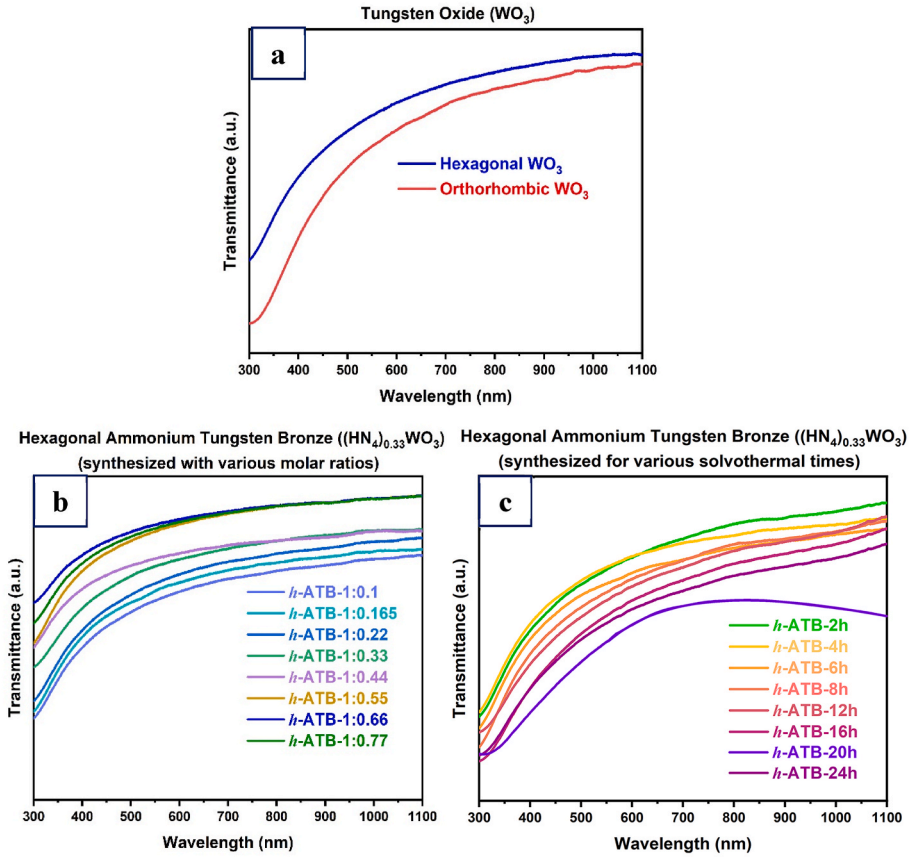

Fig. 11. Optical properties of (a) *h*-WO_3 and *β*-WO_3 prepared at 200 °C for 24 h with 15 mol/L and 30 mol/L solution molarity, (b) *h*-ATB prepared at 200 °C for 24 h with various molar ratios of W^{6+}/NH_4^+, and (c) *h*-ATB prepared at 200 °C for various solvothermal times with the molar ratio 1:0.66 of W^{6+}/NH_4^+ and solution molarity of 15 mol/L.

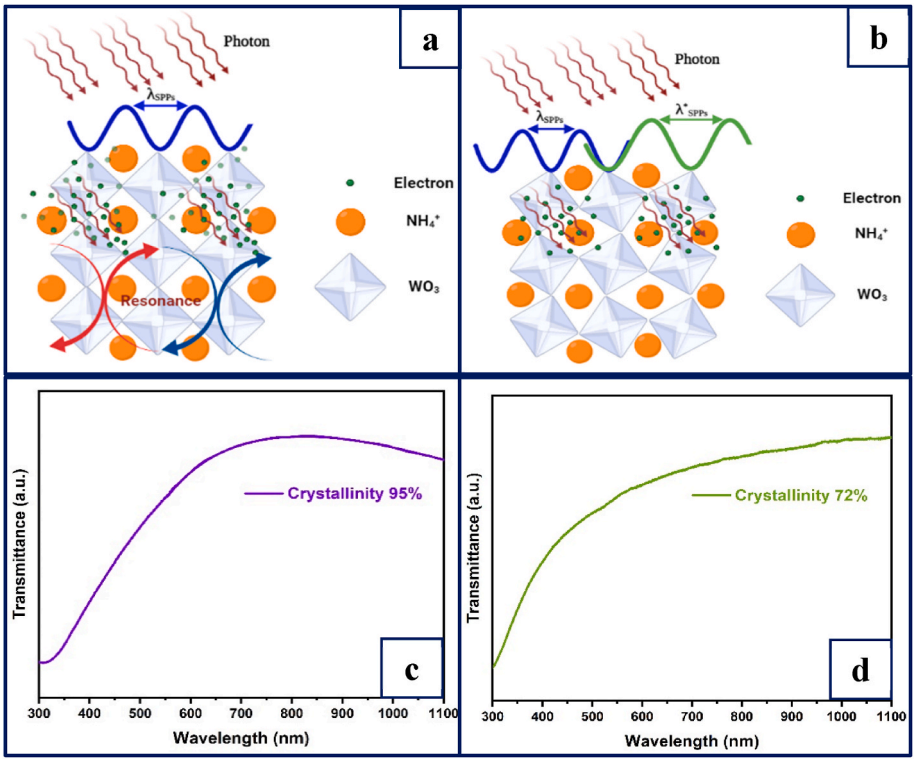

Fig. 12. Simulating possible interaction of photon and internal and surficial electron in the crystal structure of (a) *h*-ATB with high crystallinity and (b) *h*-ATB with low crystallinity, measured optical properties of (c) *h*-ATB with high crystallinity and (d) *h*-ATB with low crystallinity.

$$L_{SPPs} = \frac{1}{2k''} = \frac{\left(\varepsilon_d'\right)^2}{2\pi\varepsilon_d''\lambda_0{}^2}\left(\lambda_{SPPs}\right)^3 \quad (16)$$

$$\delta_d = \frac{\varepsilon_a}{k_0\varepsilon_d'\lambda_0{}^2}\left(\lambda_{SPPs}\right)^2 \quad (17)$$

It is observed that L_{SPPs} and δ_d affecting the near-infrared properties of the semiconductor [47,48] are proportional to λ_{SPPs}.

Therefore, a regulation model is proposed in which *h*-ATB at high crystallinity, like a grating, has significant periodicity in the crystal structure, as shown in Fig. 12(a), which can reinforce the interaction of photon and electron in the crystal structure to keep λ_{SPPs} persistence, which is more probable to dig out the near-infrared shielding nature of *h*-ATB in Fig. 12(c). In contrast, *h*-ATB at low crystallinity, like a sieve, lacks periodicity in the crystal structure, as shown in Fig. 12(b), which makes it impossible to sustain the electron-photon resonance for long, causing λ_{SPPs} to break in continuity, which is adverse to developing the potential optical feature of *h*-ATB in Fig. 12(d).

3. Conclusion

The work outlines a facile solvothermal reaction procedure for synthesizing *h*-WO_3, *β*-WO_3, and *h*-ATB in situ. Based on the first principle, the potential optical properties of *h*-WO_3 and *h*-ATB have been predicted through analysis and calculation of their electronic structures and dielectric functions. XRD testified that changing solution molarity can cause *h*-WO_3 and *β*-WO_3 phase transitions, and that varying molar ratio or solvothermal time can control the crystallinities of *h*-ATB. XPS validated that the value *x* in $(NH_4)_xWO_3$ is 0.33. SEM and TEM combining with diffraction pattern calibration observed that the synthesized *h*-ATB nanorods possess dimensions of 10–25 nm in diameter and 30–50 nm in length, and an interplanar spacing of 0.3703 nm and 0.3125 nm along the (002) and (200) crystal planes. It is attractive that *h*-ATB can obtain NIR absorption ability when crystallinity exceeds a threshold (95%), comparable to calculated results. It suggests that the change in crystallinity can adjust the optical properties of doped metal oxides.

Declaration of competing interest

The authors declare that they have no known competing financial interests or personal relationships that could have appeared to influence the work reported in this paper.

Acknowledgments

This work was supported by Yunnan Provincial Education Department Scientific Research Fund Project (2021J0055, KKJJ202107025); Kunming University of Science and Technology People Training Fund (KKZ3201907007).

References

[1] I.M. Szilàgyi, J. Madaràsz, G. Pokol, F. Hange, G. Szalontai, K. Varga-Josepovits, A. L. Tóth, The effect of K^+ ion exchange on the structure and thermal reduction of hexagonal ammonium tungsten bronze, J. Therm. Anal. Calorim. 97 (2009) 11–18.
[2] L. Tegg, D. Cuskelly, V.J. Keast, The sodium tungsten bronzes as plasmonic materials: fabrication, calculation and characterization, Mater. Res. Express 4 (6) (2017), 065703.
[3] C. Guo, S. Yin, L. Huang, L. Yang, T. Sato, Discovery of an excellent IR absorbent with a broad working waveband: Cs_xWO_3 nanorods, Chem. Commun. 47 (2011) 8853–8855.
[4] Y. Zhang, D. Guo, R.X. Li, Synthesis of $Cs_{0.3}O_3$ with visible transparency and near-infrared absorption from commercial WO_3, J. Solid State Chem. 306 (2021), 122768.
[5] L. Hernan, M. Macias, J. Morales, L. Sanchez, J. Tirado, Ion exchange of potassium hexatungstate ($K_{0.30}WO_{3.15}$) by protons, Solid State Ionics 47 (1991) 75–79.
[6] M. Mohammadi, F.R. Negreiros, T. Radlinger, P. Edelmayer, F.P. Netzer, S. Surnev, Interaction of Na with 2D WO_3 and MoO_3 layers on Pd(100): from doping to 2D bronze formation, J. Phys. Chem. C 126 (6) (2022) 3289–3300.
[7] Y. Ikeuchi, H. Takatsu, C. Tassel, Y. Goto, T. Murakami, H. Kageyama, High-Pressure synthesis of fully occupied tetragonal and cubic tungsten bronze oxides, Angew. Chem., Int. Ed. 56 (21) (2017) 5770–5773.
[8] R. Doren, B. Leibauer, M.A. Lange, E. Schechtel, L. Pradel, M. Panthofer, M. Mondeshki, W. Tremel, Gram-scale selective synthesis of WO_{3-x} nanorods and $(NH_4)_{(x)}WO_3$ ammonium tungsten bronzes with tunable plasmonic properties, Nanoscale 13 (17) (2021) 8146–8162.
[9] S. Jindal, S. Devi, K.M. Batoo, G. Kumar, A. Vasishth, Impact of copper substitution on the structural, ferroelectric and magnetic properties of tungsten bronze ceramics, Physica B Condens. Matter 537 (2018) 87–92.
[10] W. Si, Y.K. Yin, Y.P. Hu, X.X. Kang, Y.S. Xu, A.Y. Shi, B.W. Zhang, J.Y. Liu, Analysis on factors affecting the cooling effect of optical shielding in pavement coatings, Build. Environ. 211 (2022), 108766.
[11] L.M. Chao, C.W. Sun, J.X. Li, M. Sun, J. Liu, Y.H. Ma, Influence of size and shape on optical properties of cesium tungsten bronze: an experimental and theoretical approach, Ceram. Int. 48 (5) (2022) 6436–6442.
[12] L. Jin, S. Guo, R.J. Cava, $Sn_{0.24}WO_3$ hexagonal tungsten bronze prepared via the metal chloride route, J. Solid State Chem. 291 (2020), 121553.
[13] C. Pellegrini, H. Glawe, A. Sanna, Density functional theory of superconductivity in doped tungsten oxides, Phys. Rev. Mater. 3 (6) (2019), 064804.
[14] R. Cisternas, L. Ballesteros, M.L. Valenzuela, H. Kahlert, F. Scholz, Decreasing the time response of calibration-free pH sensors based on tungsten bronze nanocrystals, J. Electroanal. Chem. 801 (2017) 315–318.
[15] L. Fan, Y.Y. Xin, Y.M. Xu, X.F. Zhang, X.L. Cheng, L.H. Liu, H.Y. Song, S. Gao, L. H. Huo, Carbon nanospheres modified with WO_2-Na_xWO_3 nanoparticles for highly sensitive electrochemical detection of dopamine, Microchem. J. 170 (2021), 106770.
[16] W.T. Zhan, H.W. Ni, R.S. Chen, Z.Y. Wang, Y.W. Li, J.H. Li, One-step hydrothermal preparation of TiO_2/WO_3 nanocomposite films on anodized stainless steel for photocatalytic degradation of organic pollutants, Thin Solid Films 548 (2013) 299–305.
[17] L. Wang, J.H. Zhan, W.L. Fan, G.W. Cui, H.G. Sun, L.H. Zhuo, X.A. Zhao, B. Tang, Microcrystalline sodium tungsten bronze nanowire bundles as efficient visible light-responsive photocatalysts, Chem. Commun. (J. Chem. Soc. Sect. D) 46 (46) (2010) 8833–8835.
[18] A. Sharma, A.K. Saini, N. Kumar, N. Tejwan, T.A. Singh, V.K. Thakur, J. Das, Methods of preparation of metal-doped and hybrid tungsten oxide nanoparticles for anticancer, antibacterial, and biosensing applications, Surface. Interfac. 28 (2022), 101641.
[19] H.T. Handal, N.A.A. Ghany, S.A. Elsherif, A. Siebel, N.K. Allam, Unraveling the structure and electrochemical supercapacitive performance of novel tungsten bronze synthesized by facile template-free hydrothermal method, Electrochim. Acta 401 (2022), 139494.
[20] B. Wang, Q.J. Wang, Y.T. Zhu, L.T. Kang, J.X. Zhu, F.Y. Jiang, W. Du, D.J. You, Z. T. Zhang, F. Gao, A photo-/thermo-dual-responsible Cs_xWO_3/PNIPAM composite hydrogel for energy-efficient windows, Mater. Res. Express 6 (8) (2019), 085708.
[21] J. Guo, X.F. Lu, C.J. Gao, X.Q. Hou, Effects of element A on the crystal structure of tungsten bronzes A_xWO_3, J. Funct. Mater. 46 (17) (2015) 17008–17013.
[22] F. Krumeich, The complex crystal chemistry of niobium tungsten oxides, Chem. Mater. 34 (3) (2022) 911–934.
[23] H. Yin, Y. Kuwahara, K. Mori, C. Louis, H. Yamashita, Properties, fabrication and applications of plasmonic semiconductor nanocrystals, Catal. Sci. Technol. 10 (13) (2020) 4141–4163.
[24] L. Tegg, D. Cuskelly, V.J. Keast, The sodium tungsten bronzes as plasmonic materials: fabrication, calculation and characterization, Mater. Res. Express 6 (4) (2017), 06570.
[25] I.M. Szilagyi, I. Sajo, P. Kiraly, G. Tarkanyi, A.L. Toth, A. Szabo, K. Varga-Josepovits, J. Madarasz, G. Pokol, Phase transformations of ammonium tungsten bronzes, J. Therm. Anal. Calorim. 98 (3) (2009) 707–716.
[26] P. Ou, X.H. Su, Y. Zeng, F.F. Zhang, J.H. Liu, C. Wang, S.H. Yang, H.B. Wang, Y. F. Wen, H.J. Zhao, Two-step hydrothermal synthesis of $(NH_4)_{(x)}WO_3$ hollow spherical and hierarchical structures, CrystEngComm 23 (8) (2021) 1700–1703.
[27] X.G. Luo, S.B. Zhu, X.H. Su, J.G. Huang, Z.K. Zhou, Q.Y. Zhou, Y.F. Wen, P. Ou, Synthesis of $(NH_4)_xWO_3$ nanorods by a novel hydrothermal route, Mater. Tehnol. 54 (2) (2020) 227–231.
[28] L. Tegg, D. Cuskelly, V.J. Keast, Plasmon responses in the sodium tungsten bronzes, Plasmonics 13 (2) (2018) 437–444.
[29] S. Yoshio, K. Adachi, Polarons in reduced cesium tungsten bronzes studied using the DFT plus U method, Mater. Res. Express 6 (2) (2019), 026548.
[30] E. Plekhanov, N. Bonini, C. Weber, Calculating dynamical mean-field theory forces in ab initio ultrasoft pseudopotential formalism, Phys. Rev. B 104 (21) (2021), 235131.
[31] C. Benhalima, S. Amari, L. Beldi, B. Bouhafs, First-Principles study of ferromagnetism in iron chromite spinels: $FeCr_2O_4$ and $CrFe_2O_4$, Spin 9 (3) (2019), 1950014.
[32] H.H. Yang, H.G. Sun, Q.T. Li, P. Li, K.K. Song, B. Song, L. Wang, Structural, electronic, optical and lattice dynamic properties of the different WO_3 phases: first-principle calculation, Vacuum 164 (2019) 411–420.
[33] H. Jin, H.G. Zhou, Y.F. Zhang, Theoretical investigations on the structural and electronic properties of WO_3 polymorphs, Chin. J. Struct. Chem. 37 (12) (2019) 1878–1890.
[34] M. Mansouri, T. Mahmoodi, Ab initio investigation on the effect of transition metals doping and vacancies in WO_3, Acta Phys. Pol. A 129 (1) (2016) 8–14.
[35] S. Pourmasoud, M. Eghbali-Arani, A.A. Arani, Electronic and optical properties of UPtGe crystal, J. Phys. Chem. Solid. 166 (2022), 110703.

[36] M. Gajdoš, K. Hummer, G. Kresse, J. Furthmüller, F. Bechstedt, Linear optical properties in the projector-augmented wave methodology, Phys. Rev. B 73 (2006), 045112.
[37] H.H. Yang, H.G. Sun, Q.T. Li, P. Li, K.K. Song, B. Song, L. Wang, Structural, electronic, optical and lattice dynamic properties of the different WO_3 phases: first-principle calculation, Vacuum 164 (2019) 411–420.
[38] B.S. Zhou, H.R. Gao, Y.C. Liu, Z.M. Li, Y.Y. Huang, F.C. Liu, X.C. Wang, First principles investigation on Li or Sn codoped hexagonal tungsten bronzes as the near-infrared shielding material, Chin. Phys. B 31 (5) (2022), 057804.
[39] Q.Y. Xu, L.H. Xiao, J.Y. Ran, R. Tursun, G.D. Zhou, L.L. Deng, D.S. Tang, Q.W. Shu, J.Y. Qin, G.S. Lu, P. Peng, $Cs_{0.33}WO_3$ as a high-performance transparent solar radiation shielding material for windows, J. Appl. Phys. 124 (19) (2018), 193102.
[40] J. Sun, H.T. Wang, J.L. He, Y.J. Tian, Ab initio investigations of optical properties of the high-pressure phases of ZnO, Phys. Rev. B 72 (12) (2005), 125132.
[41] C.Q. Liu, Q.W. Shu, J.Y. Qin, Y. Yuan, W. Qiu, P. Peng, L.H. Xiao, Predictions of electronic structures and optical performance of potential near infrared absorber $Sn_{0.33}WO_3$, AIP Adv. 9 (11) (2019), 115014.
[42] N. Stojilovic, Why can't we see hydrogen in X-ray photoelectron spectroscopy? J. Chem. Educ. 89 (10) (2012) 1331–1332.
[43] Y. Bai, J.Z. Zhao, Z.L. Lv, K. Lu, Enhanced piezocatalytic performance of ZnO nanosheet microspheres by enriching the surface oxygen vacancies, J. Mater. Sci. 55 (29) (2020) 14112–14124.
[44] Q.H. Zhu, K. Zhang, D.Q. Li, N. Li, J.K. Xu, D.W. Bahnemann, C.Y. Wang, Polarization-enhanced photocatalytic activity in non-centrosymmetric materials based photocatalysis: a review, Chem. Eng. J. 426 (2021), 131681.
[45] Q.H. Zhu, R. Hailili, Y. Xin, Y.T. Zhou, Y. Huang, X.Z. Pang, K. Zhang, P.K. J. Robertson, D.W. Bahnemann, C.Y. Wang, Efficient full spectrum responsive photocatalytic NO conversion at $Bi_2Ti_2O_7$: Co-effect of plasmonic Bi and oxygen vacancies, Appl. Catal., B 319 (15) (2022), 121888.
[46] H. Raether, Surface Plasmons on Smooth and Rough Surfaces and Gratings, Springer-Verlag, Berlin, 1988.
[47] A.V. Zayatsa, I.I. Smolyaninov, A.A. Maradudin, Nano-optics of surface plasmon polaritons, Phys. Rep. 408 (2005) 131–314.
[48] W.J. Wang, W.H. Lin, Optical properties of plasmonic components based on a nanoscale three-dimensional plasmonic waveguide, J. Opt. Soc. Am. B 36 (8) (2019) 2045–2051.